Excited-State Mixed Valence in a Diphenyl Hydrazine Cation: Spectroscopic Consequences of Coupling and Transition Dipole Moment Orientation

Jenny V. Lockard and Jeffrey I. Zink*

Department of Chemistry and Biochemistry, University of California, Los Angeles, California 90095

Dwight A. Trieber II, Asgeir E. Konradsson, Michael N. Weaver, and Stephen F. Nelsen*

Department of Chemistry, University of Wisconsin, 1101 University Avenue, Madison, Wisconsin 53706-1396

Received: November 17, 2004

A quantitative model of mixed-valence excited-state spectroscopy is developed and applied to 2,3-diphenyl-2,3-diazabicyclo[2.2.2]octane. The lowest-energy excited state of this molecule arises from a transition from the ground state, where the charge is located on the hydrazine bridge, to an excited state where the charge is associated with one phenyl group or the other. Coupling splits the absorption band into two components with the lower-energy component being the most intense. The sign of the coupling, derived by using a neighboring orbital model, is positive. The transition dipole moments consist of parallel and antiparallel vector components, and selection rules for each are derived. Bandwidths are caused by progressions in totally symmetric modes determined from resonance Raman spectroscopic analysis. The absorption, emission, and Raman spectra are fit simultaneously with one parameter set.

Introduction

Excited-state mixed valence exists when a system possesses two or more interchangeably equivalent sites that have different oxidation states in an excited electronic state but a symmetrical charge distribution in the ground electronic state. Some of the most commonly encountered molecular systems having these characteristics contain two identical charge-bearing units M separated by a bridge B and are represented in this paper by the generic M−B−M symbol. The first mixed-valence excited state that was examined in detail was that of a dication where the symmetric charge distribution M^+-B-M^+ in the ground state is changed after an electronic transition to a distribution that isolates the entire charge on either one charge-bearing unit or the other, $M^{2+}-B-M/M-B-M^{2+}$. This rare type of transition was the focus of an earlier study of ours in which we presented the first quantitative treatment of a mixed-valence excited state and its spectroscopic ramifications.[1] The example for that analysis was a durene-bridged dihydrazine dication, Hy−DU−Hy^{2+}. The two most important results are that the absorption band consists of two components separated in energy by twice the effective coupling in the excited electronic state and that the selection rules are governed by the directions and signs of the transition dipole moments.

The focus of this paper is an M−B−M monocation, the diphenyl hydrazine radical cation **1**$^+$ (**22/Ph$_2$**$^+$). The phenyl rings are twisted such that the point group is C_2. In the ground state, the charge is located on the bridge, $M-B^+-M$.

The mixed-valence excited state occurs when the charge is transferred from the bridge to one M or the other, which produces two localized configurations: M^+-B-M and $M-B-M^+$. In this example, M is a phenyl group and is the charge-bearing unit in the excited state, and the bridge, B, is a substituted hydrazine radical cation. Because the two M groups

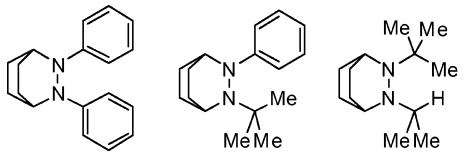

1: 22/Ph$_2$ **2: 22/PhtBu** **3: 22/tBuiPr**

are coupled to each other through the bridge, the excited state can be modeled using the language of the Marcus−Hush theory, usually used to describe ground-state intervalence behavior.[2,3] Instead of a ground and one excited-state surface, there are two excited-state surfaces separated in energy at $Q = 0$ by twice the excited-state coupling element H_{ab}^{ex}. While the difference between ground- and excited-state mixed valence may appear subtle, the spectroscopy of the two systems reveals striking dissimilarities, because excited-state mixed-valence systems involve electronic transitions from the $M-B^+-M$ ground state to the coupled $M^+-B-M/M-B-M^+$ excited state, whereas for ground-state intervalence systems, the transitions occur within the coupled $M^+-B-M/M-B-M^+$ system.

The electronic spectra of diphenyl hydrazine radical cation **1**$^+$ (**22/Ph$_2$**$^+$) and its monophenyl analogue **2**$^+$ (**22/tBuPh**$^+$) show initially surprising differences that provide a prototypical example of excited-state mixed-valence spectra. The diphenyl compound has two phenyl-to-hydrazine charge transfer absorptions, while the monophenyl compound has one band roughly midway between those of the diphenyl compound. In simplest terms, the two bands in the diphenyl compound's spectrum are caused by excited-state splitting. Instead of the single ground-to-excited-state absorption of the monophenyl compound, absorptions to both an upper and lower split excited-state energy level occur.

Electronic transitions to mixed-valence excited states are treated quantitatively in this paper using the time-dependent theory of spectroscopy,[4−8] specifically applied to coupled

* E-mail: zink@chem.ucla.edu (J.I.Z.), nelsen@chem.wisc.edu (S.F.N.).

10.1021/jp044750x CCC: $30.25
Published on Web 01/26/2005

electronic states.[9,10] Previous applications of the theory include intensity borrowing caused by coupled states, absorption and emission spectra of coupled states in transition metal compounds,[11−13] interference dips (i.e., the decrease of absorbance in a broad absorption band at the position of a second absorption band)[14−19] and ground-state intervalence electron-transfer spectroscopy.[20−22] All of these applications involve the propagation of wave packets on multiple coupled excited-state surfaces; they cannot be interpreted in terms of diabatic or adiabatic Born−Oppenheimer potential energy surfaces, because the nuclear kinetic energy must be included.

In this paper, we explain the features of the electronic spectra of the hydrazine radical cations using an excited-state mixed-valence potential energy surface model. The transition to the coupled excited state results in an observed absorption band that has two peaks, with the less intense peak at higher energy. In fitting the spectrum, the energy separation between the two peak maxima is determined by the magnitude of coupling between the excited-state surfaces in the model. The intensity ratio of the two peaks is dictated by four factors: the magnitude of the coupling, the sign of the coupling, the spatial orientation between the transition dipoles in the nonlinear molecule, and the relative signs of the transition dipoles. The importance of the sign of the effective coupling is surprising; the properties of ground-state mixed-valence molecules are not dependent on the sign. The sign of the coupling in the mixed-valence excited state of the diphenyl hydrazine radical cation $\mathbf{1}^+$ is positive. We present a brief orbital symmetry analysis to explain the origin of the positive sign. The transition dipole moments in this nonlinear system can be split into parallel (same direction) and antiparallel (opposite direction) vector components. We derive the relative magnitudes of the components of the spectra resulting from these parallel and antiparallel vector components of the transition dipole moments. Emission from the coupled excited state to the ground state is observed at low temperature. Resonance Raman spectra are used to determine the frequencies and displacements of the totally symmetric normal modes that undergo changes between the ground and excited electronic state. These modes, together with the asymmetric mode that is important when the charge is transferred to each of the phenyl groups, are used to fit both the emission and absorption spectra of $\mathbf{1}^+$. The electronic spectra are calculated by using the time-dependent theory of spectroscopy and methodology developed to calculate spectra involving coupled surfaces. The absorption, emission, and Raman spectra are fit simultaneously with one parameter set. In addition to the parameters that define these coupled surfaces, we discuss in detail the treatment of the parallel and antiparallel vector components of the dipole moment for transitions to these surfaces.

Experimental Section

1. Synthesis. Preparations of **2** (**22/PhtBu**),[23] and **3** (**22/iPr$_2$**)[24] have been previously published.

*2,3-Diphenyl-2,3-diazabicyclo[2.2.2]octane (**1**, **22/Ph$_2$**).* In a 25-mL round-bottom flask, 2,3-diazabicyclo[2.2.2]oct-2-ene (970 mg, 8.82 mmols) is dissolved in 10 mL THF and cooled to −78 °C. The solution is purged with argon for 30 min, during which some of the azo compound precipitates. To that clear and colorless solution, 7.4 mL of PhLi (1.8 M in 70:30 cyclohexane/Et_2O, 13.22 mmol) are added over a period of 2 min. The resulting red−purple solution is stirred at −78 °C for 30 min and then at room temperature for a further 60 min. The solution is added by cannula dropwise into an Et_2O solution of I_2 (5.08 g, 20.0 mmols in 40 mL Et_2O). Heat evolves during the addition, and an orange solid forms immediately. The azo flask is washed with 2 mL THF that is also cannulated into the I_2 solution. The resulting suspension is stirred under N_2 at room temperature and then carefully vacuum-filtered. The resulting solid is washed three times with Et_2O and air-dried, giving 2.30 g (83%) of crude 2-phenyl-2,3-diazabicyclo[2.2.2]oct-2-ene iodide: ^{1}H NMR (CD_3CN) δ 1.71−1.95 (m, 4H), 2.25−2.40 (m, 4H), 6.02 (bs, 1H), 6.07 (bs, 1H), 7.75 (t, 2H), 7.90 (t, 1H), 8.10 (d, 1H). ^{13}C NMR (CD_3CN) δ 24.38, 26.04, 69.30, 69.93, 123.81, 131.42, 115.0. This material (1.413 g, 4.5 mmol) is placed in a 25-mL round-bottom flask under N_2, cooled to 0 °C, and then, 10 mL of *n*-pentane is added. The suspension is stirred, and 3.7 mL of PhLi (1.8 M in 70:30 cyclohexane/Et_2O, 6.7 mmol) is added dropwise via syringe. Reaction is immediate, and the solution is stirred for 30 min at 0 °C and then at room temperature. A 10-mL quantity of Et_2O is added to wash some of the solid down the sides of the flask. After 4.5 h, the reaction is quenched by adding 50 mL of MeOH, then 5 mL of concentrated HCl. Not all of the solid dissolves, so the solution is carefully extracted with 2 × 30 mL of pentane. The pentane is back-extracted with H_2O and filtered. White solid collected from the pentane washings is combined with the aqueous phase, which is then basified (pH > 10) with KOH pellets. The basic aqueous solution is extracted with 4 × 20 mL of CH_2Cl_2, and the combined CH_2Cl_2 fractions are dried over $MgSO_4$ and filtered. The solvent is removed by rotary evaporation to yield 1.34 g of a reddish-brown solid. The solid was purified by column chromatography and recrystallized from ethyl acetate to give 0.80 g (67%) of **1** as a white solid, mp 203−204 °C (lit.[25] 205−206 °C). The identity was further verified by X-ray crystallography (See Supporting Information).

*2,3-Diphenyl-2,3-diazabicyclo[2.2.2]octane Radical Cation Hexafloroantiminate (**1**$^+$**SbPF$_6^-$**).* In a flame-dried 10-cm test tube were placed $AgSbF_6$ (42.7 mg, 0.124 mmols) and **1** (36.0 mg, 0.136 mmols, 1.1 equiv). The test tube was purged with N_2 for 15 min and then cooled to −78 °C. In a second flame-dried 10-cm test tube, CH_2Cl_2 (freshly distilled from CaH_2 and passed over ∼10−12 cm of activated basic Al_2O_3) was placed and also cooled to −78 °C under N_2. When both test tubes had cooled (∼15 min), approximately 2 mL of CH_2Cl_2 was added by cannula into the hydrazine/silver test tube. The resulting solution, which immediately began turning purple and continued darkening for at least 20 min, was stirred, at −78 °C for 30 min, then removed and stirred for a further 30 min at room temperature. A silver mirror had formed on the sides of the test tube, which was then sonicated for 10 min and stirred for 15 min, and the solution was then filtered into a clean test tube, through a 2-cm column packed with Celite. The reaction tube was washed twice with 0.5 mL of CH_2Cl_2 (filtrate was colorless after the second washing), and the washings were filtered and combined with the original filtrate. The combined filtrate was partitioned into three 10-mm test tubes, and dark purple crystals precipitated from each with vapor diffusion of Et_2O at −20 °C over 2 days. The resulting crystals were washed with Et_2O and dried in a vacuum oven at 60 °C. Decomposition begins at 196 °C. The compound was characterized by X-ray crystallography (see Supporting Information).

2. Electronic Spectroscopy. Absorption spectra taken of acetonitrile solution samples at room temperature were obtained using a Perkin-Elmer Lambda 20 UV−vis spectrophotometer. Emission spectra taken of the samples in a frozen acetonitrile solvent matrix at 15 K were obtained using a Spex 1702 single monochromator equipped with a Burle C31034 photomultiplier tube. The signal was recorded with a Stanford Research System

SR400 photon counter and processed by a computer. The 406-nm line of a Coherent I-300 Krypton laser at 4 mW was used for excitation. The acetonitrile solution sample was cooled using an Air Products closed-cycle helium refrigerator displex equipped with a thermocouple. The spectrum was corrected for instrument response.

3. Raman Spectroscopy. Spectra were obtained using a triple monochromator equipped with a Princeton Instruments LN-CCD. Data were processed by a PC computer. The 568- and 407-nm lines of a Coherent I-300 Krypton laser at ~100 mW were used for excitation. The spectra were collected from a spinning pressed pellet of potassium nitate and $\mathbf{1}^+$.

Theoretical and Numerical Methods

The *Gaussian 98* program suite was used for B3LYP/6-31+G* calculations,[26,27] *Jaguar* for the B3LYP/6-31++G** frequency calculation,[28] and *Spartan '02* for B3LYP/6-31G* calculations.[29] Standard Pople-style basis sets and all correlation methods were used as implemented within the respective program suites. Geometry optimizations were performed using standard gradient methods. Frequency calculations were conducted on optimized geometries to confirm that a minimum had been located on the potential energy surface. Geometries obtained through *Gaussian 98* calculations were viewed using the MOLDEN software package for viewing molecular density.[30]

Electronic spectra for excited-state mixed-valence potential surfaces are calculated in the framework of the time-dependent theory of molecular spectroscopy. The theoretical foundation underlying these calculations has been described previously.[4−6,31] In this section, the theory underlying the calculation of electronic spectra for coupled potential surfaces is briefly presented.

1. Absorption Spectra. The fundamental equation for the calculation of an absorption spectrum in the time-dependent theory is

$$I(\omega) = C\omega \int_{-\infty}^{+\infty} \exp(i\omega t)\left[\langle\Phi|\Phi(t)\rangle \exp\left(-\Gamma^2 t^2 + \frac{iE_o}{h}t\right)\right] dt \quad (1)$$

with $I(\omega)$ as the absorbance at frequency ω, E_o the energy of the electronic origin transition, and Γ a phenomenological Gaussian damping factor.[8] The damping factor arises because of relaxation into other modes (such as low-frequency solvent modes with small distortions) and the "bath". The effect of increasing Γ on the spectrum in the frequency domain is to decrease the resolution, that is, to "fill in" the spectrum. The most important part of eq 1 is $\langle\Phi|\Phi(t)\rangle$, the autocorrelation function of the wave packet Φ prepared on an excited-state potential surface after the spectroscopic transition, with the wave packet $\Phi(t)$ developing on this surface with time. In the absence of coupling terms between the normal coordinates, the total autocorrelation in a system with K coordinates is given by

$$\langle\Phi|\Phi(t)\rangle = \prod_k \langle\phi^k|\phi^k(t)\rangle \quad (2)$$

where ϕ^k is a wave packet associated with coordinate k ($k = 1, ..., K$) and is a two-dimensional vector: $\phi^k(Q_k, j)$, where Q_k is the coordinate along mode K and $j = 1, 2$ is an index over the two electronic states. In the following, we will eliminate the index k and consider only a single coordinate. The $t = 0$ wave packet is then defined as

$$\phi(t = 0) = \mu\chi_i \quad (3)$$

or, more explicitly,

$$\phi(Q, j, t = 0) = \sum_{j=1}^{2} \mu_j(Q)\chi_i(Q) \quad (4)$$

Here, the subscript i denotes the initial state; χ_i is the lowest-energy ground-state eigenfunction. We do not label ϕ by the initial state index i to avoid cluttering with indices, but the wave packet depends on the initial state. The signs of the transition dipole moments μ_j ($j = 1, 2$) depend on the direction of the electron transfer. For antiparallel transitions, the signs are opposite, and for parallel transitions, they are the same.

The diagonal elements, H_j's, of the Hamiltonian are

$$H_j = -\frac{1}{2M}\nabla^2 + V_j(Q) \quad (5)$$

where $V_j(Q)$ is the potential energy as a function of the configurational coordinate Q and $-1/2M\cdot\nabla^2$ is the nuclear kinetic energy.

When two coupled surfaces that represent the excited state are involved, we need to keep track of two wave packets, ϕ_1 and ϕ_2, moving on the two coupled potential surfaces.[32−34] The wave packet $\phi(t)$ is given by the time-dependent Schrödinger equation:

$$i\frac{\partial}{\partial t}\begin{pmatrix}\phi_1\\ \phi_2\end{pmatrix} = \begin{pmatrix}H_1 & V_{12}\\ V_{21} & H_2\end{pmatrix}\begin{pmatrix}\phi_1\\ \phi_2\end{pmatrix} \quad (6)$$

(where now the subscript denotes the electronic state, $j = 1$ or 2), the diagonal elements H_j's of the total Hamiltonian are given in eq 5, and $V_{12} = V_{21}$ is the coupling between the two diabatic potentials. The total overlap $\langle\phi\ |\phi(t)\rangle$ is calculated as

$$\langle\phi|\phi(t)\rangle = \langle\phi_1|\phi_1(t)\rangle + \langle\phi_2|\phi_2(t)\rangle \quad (7)$$

For simplicity, we chose harmonic potentials in all of the following examples, although the methods used are not restricted by the functional form of the potentials. The displacement of the minimum of one electronic state from the other, from that of the ground state, ΔQ, is abbreviated as Δ in this paper. The potentials are given by

$$V_j(Q) = \frac{1}{2}k_j(Q \pm \Delta Q_j)^2 + E_j \quad (8)$$

with $k_j = 4\pi^2 M(h\omega_j)^2$ as the force constant, ΔQ_j the positions of the potential minima along Q, and E_j the energy of the potential minimum for state j. These uncoupled potentials are illustrated in part 1 of the Discussion section. The coupling between the diabatic potentials for states 1 and 2 is chosen to be coordinate-independent in this paper, although the computational method allows us to use coordinate-dependent coupling. Note that different authors use the symbols for the coupling V_{12} or H_{ab} or ϵ interchangeably. The symbol H_{ab} is used in the remainder of this paper, because H_{ab} is most commonly found in discussions of organic compounds. For excited states, the symbol H_{ab}^{ex} is used, and the superscript denotes coupling in the excited electronic state.

2. Emission Spectra. The fundamental equation for the calculation of an emission spectrum in the time-dependent theory is similar to that for the absorption spectrum calculation:

$$I(\omega) = C\omega^3 \int_{-\infty}^{+\infty} \exp(i\omega t)\left[\langle\Phi|\Phi(t)\rangle \exp\left(-\Gamma^2 t^2 + \frac{iE_0}{h}t\right)\right] dt \quad (9)$$

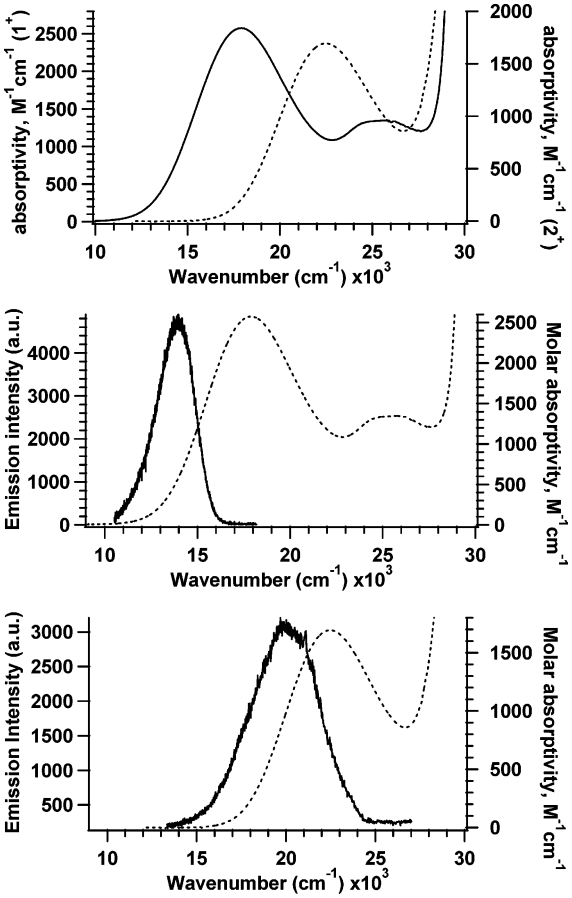

Figure 1. (Top) absorption spectra of $\mathbf{2}^+$ and $\mathbf{1}^+$. Absorption and emission spectra of (middle) $\mathbf{1}^+$ and (bottom) $\mathbf{2}^+$.

For emission spectroscopy, the wave packet originates from the coupled excited-state surfaces and is propagated on the ground-state surface. The calculation of the autocorrelation function $\langle\phi|\phi(t)\rangle$ requires the appropriate initial wave packet, ϕ ($t = 0$), and, by eq 3, χ_i, the lowest-energy eigenfunction of the coupled excited-state surfaces. The eigenfunction has two components, one from each of the diabatic surfaces. The eigenfunction is calculated as follows

$$\chi_i = \text{const} \int_0^T \eta(t) w(t) \exp\left(\frac{iE_i}{h} t\right) \mathrm{d}t \qquad (10)$$

where χ_i denotes the eigenfunction corresponding to the eigenvalue E_i, $\eta(t)$ is the time-dependent (propagating) wave function, which initially is located arbitrarily on the surface, and $w(t)$ is a Hanning window function. Note that, for coupled potentials, each eigenfunction χ_i is an array with two components corresponding to the two diabatic potentials that form the basis in the calculations (i.e., χ_i is specifically $\chi_i(Q, j)$.

Results

The absorption spectra of the diphenyl radical cation, $\mathbf{1}^+$, and the monophenyl analogue, $\mathbf{2}^+$, are shown in Figure 1. The lowest-energy absorption band of $\mathbf{1}^+$ consists of two components at 17 900 and 25 900 cm^{-1}. A higher-energy absorption band occurs with peak maximum at 29 600 cm^{-1}. The lowest-energy absorption band of $\mathbf{2}^+$ consists of a single peak with band maximum at 22 500 cm^{-1}. The low-temperature emission spectrum of $\mathbf{1}^+$ in acetonitrile glass, shown in Figure 1, consists of an unstructured band with its maximum at 14 215 cm^{-1} and a full-width at half-maximum (fwhm) of 2230 cm^{-1}.

TABLE 1: Expermental and Calculated Vibrational Data for $\mathbf{1}^+$

Raman $\bar{\nu}$ (cm^{-1}) [a]	calcd vibration (cm^{-1}) [b]	exptl Raman intensity, I_R [a]	Δ [c]	λ_q^{ex} (cm^{-1}) [d]	assignment
291	294, 295	0.1859	0.78	88	CNNC twist
423	418, 419	0.5274	0.91	175	CNNC twist
487	493, 491	0.4942	0.76	140	CNNC twist
512	513, 518	0.4107	0.66	111	CNNC twist
604	609, 612	0.0827	0.25	18	CNNC twist
619	628, 628	0.1422	0.32	31	Ph def. and N bend
730	736, 737	0.1904	0.32	37	Ph def. and CN, NN str.
836	833, 847	0.1759	0.26	28	Ph rock
919	932, 936	0.1203	0.2	18	Ph deformation
1005	1017, 1015	0.1996	0.23	26	Ph deformation
1188	1203, 1208	0.7405	0.38	85	CN stretch
1205	1222, 1226	0.4997	0.31	101	CN stretch
1273	1294, 1297	0.9351	0.4	101	22 ring + NN
1346	1332, 1342	0.3687	0.4	107	Ph CC stretch
1413	1433, 1437	1.0333	0.48	162	NN stretch
1489	1514, 1526	1.6606	0.31	71	Ph CC stretch
1586	1627, 1634	0.7532	0.38	114	Ph CC stretch

[a] Excitation energy, 568 nm. [b] Calculated at UB3LYP/6-31++G** and UB3LYP/6-31+G* [c] Dimensionless distortions obtained from resonance Raman intensities using Savin's formula.[8] [d] Increments to λ_V^{ex}, calculated as $^1/_2\bar{\nu}\Delta^2$.

TABLE 2: Comparison of the Structural Data for 22/Ph$_2^+$ ($\mathbf{1}^+$) Obtained from the X-ray Crystal Structures of the SbF$_6^-$ Salt and UB3LYP/6-31+G* Calculation on It and 22/PhtBu$^+$ ($\mathbf{2}^+$)

compound	**22/Ph$_2$** X-ray	**22/Ph$_2^+$SbF$_6$** X-ray	**22/Ph$_2^+$** UB3LYP	**22/PhtBu$^+$** UB3LYP
d(NN) (Å)	1.443 (2)	1.348 (2)	1.358	1.358
d(CN) (Å)	1.413 (2)	1.421 (3), 1.426 (3)	1.429	1.439
$\Delta\alpha_{av}(N_4)$ (°)	5.9 (2)	1.2 (2), 1.4 (2)	1.5	1.7
$\angle C_{Ar}NNC_{Ar}$ (°)	110.3 (2)	46.7 (3)	50.1	58.3
$\angle C_HNNC_H$ (°)	21.8 (2)	2.8 (3)	2.8	6.6
ϕ(NC$_{Ar}$) (°)	17.8 (2)	36.0 (3), 34.7 (3)	42.3, 42.3	61.0

The observed resonance Raman frequencies (in wavenumbers) and the integrated intensities for those modes (normalized to the intensity of the 1055 cm^{-1} nitrate peak of the standard) obtained using 568-nm (16 706 cm^{-1}) excitation are summarized in Table 1. The bands listed have an intensity of at least 5% of that of the most intense band at 1413 cm^{-1}. The calculated frequencies for the vibrational modes assigned to the experimental resonance Raman band also appear in Table 1.

X-ray structures of neutral **1** and its SbF$_6^-$ salt were obtained and are compared with the structure obtained using hybrid density functional theory (DFT) Hartree−Fock B3LYP/6-31+G* calculations in Table 2. The geometry change between **1** and $\mathbf{1}^+$ is similar to that found for **2**, $\mathbf{2}^+$, and other hydrazines.[35]

Because the electronic interaction between the NN$^+$ and phenyl groups scales approximately as the cosine of the lone-pair aryl carbon p-orbital twist angle ϕ, it is important to have this angle estimated rather well. The ratio of cosines for the X-ray to the UB3LYP calculated value is 1.11, but it is not clear which value is more likely to represent the twist of the free ion in solution; crystal packing forces can change such twist angles significantly, although it appears from work on localized intervalence aryldihydrazines that they frequently do not.[35]

Discussion

1. Assignment. Both components of the lowest-energy absorption band of $\mathbf{1}^+$ are assigned to a transition from the ground state, where the unpaired electron resides on the

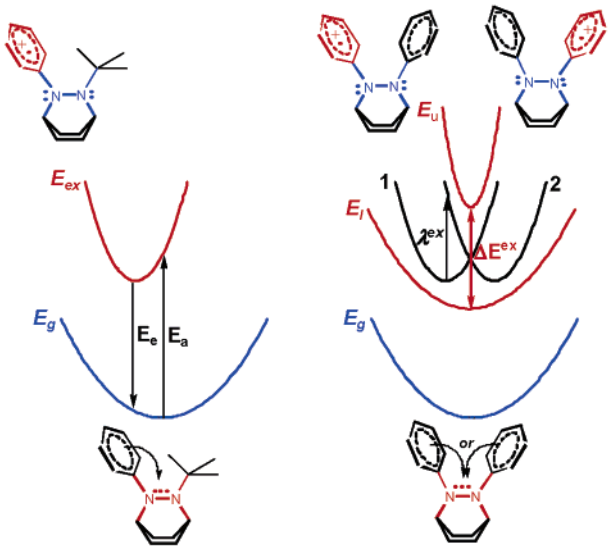

Figure 2. Ground- and excited-state potential energy surfaces for (left) phenyl-to-NN^+ electron transfer in the monophenyl hydrazine (C_s point group) and (right) excited-state splitting in the diphenyl hydrazine cation, $\mathbf{1}^+$ (C_2 point group). Diabatic surfaces represent the excited state with the positive charge on the left (1) and the right (2). Upper (E_u) and lower (E_l) adiabatic surfaces are also shown.

hydrazine unit, to a coupled excited state where the unpaired electron is located on one phenyl group or the other. This phenyl-to-hydrazine charge transfer assignment is supported by molecular orbital (MO) calculations, which give predominantly phenyl π character to the HOMO and mostly N−N π^* character to the LUMO. The absorption band of $\mathbf{1}^+$ at 29 600 cm^{-1} is assigned as an $(NN)^+$ $\pi-\pi^*$ transition. The latter assignment is supported by the comparison of the spectrum of $\mathbf{1}^+$ to that of the saturated hydrazine, $\mathbf{3}^+$ (**22/tBuiPr**). The lowest-energy band of this aliphatic-substituted hydrazine has its band maximum at ~33 800 cm^{-1} and is assigned to the $(NN)^+$ $\pi-\pi^*$ transition. Although this band is over 3000 cm^{-1} higher in energy than the $(NN)^+$ $\pi-\pi^*$ band **22/Ph$_2$**$^+$, it has been shown that the exact position of this band is very sensitive to the nature of the substituents at N.[36]

2. Excited-State Mixed Valence. The excited-state mixed-valence behavior of the diphenyl molecule (C_2 symmetry) is modeled by two interacting harmonic potential energy surfaces in the excited state as shown in Figure 2. A single harmonic surface with its minimum at zero along the normal vibrational coordinate represents the ground state with the charge localized on the nitrogens. Two possible electronic transitions from the phenyl group to the hydrazine unit send the +1 charge to one phenyl group or the other. Symmetry requires that these transitions be equal in energy and occur with equal probability. In the model, these energetically equal transitions give rise to two diabatic surfaces in the excited state that are degenerate at $Q = 0$, each representing the system with the charge localized on one phenyl. The excited-state diabatics are displaced from the ground-state surface such that the Franck−Condon region of each diabatic has a nonzero slope that is equal in magnitude and opposite in sign. The diabatic surfaces couple, creating two new nondegenerate adiabatic surfaces (upper and lower curves) with an energy splitting of ΔE^{ex} at $Q = 0$ between the lower- and higher-energy adiabatic surfaces. The degree of charge delocalization in the excited state is dictated by the ratio of ΔE^{ex} to λ^{ex}. In Figure 2, ΔE^{ex} is sufficiently large to produce a single minimum in the lower adiabatic, that is, $H_{ab}^{ex} > \lambda^{ex}/2$. The surfaces are depicted along an asymmetric normal coordinate.

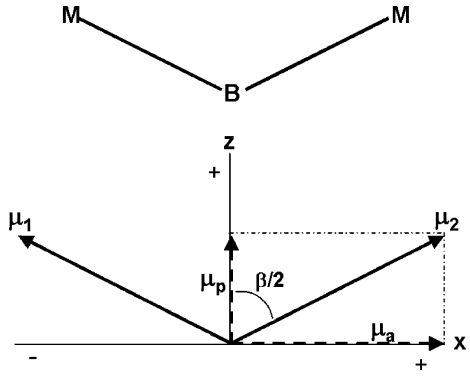

Figure 3. Components of μ for transition dipole moments of an M−B−M-type molecule.

The absorption spectrum of $\mathbf{1}^+$, as shown in Figure 1, reveals the effects of coupling along this asymmetric coordinate in the excited state. The two absorption band components at 17 900 and 25 900 cm^{-1} correspond to the transition to the lower and upper adiabatic surface, respectively. The difference in energy between the two peak maxima, therefore, is directly related to the coupling along the asymmetric coordinate involved in the excited state. If the coupling had been zero, a single peak would have been observed in the absorption spectrum, because the transition to one diabatic surface produces the same spectrum as a transition to the other. This "zero-coupling" case is illustrated analogously by the absorption spectrum of **22/PhtBu**$^+$, $\mathbf{2}^+$, also shown in Figure 1. Because only one phenyl−hydrazine transition is possible, its excited state can be modeled by one displaced harmonic surface. Consequently, the lowest-energy absorption band of $\mathbf{2}^+$ consists of a single peak at 22 500 cm^{-1} that is between the energies of the two peaks of **22/Ph$_2$**$^+$.

3. Transition Dipole Moments. The transition dipole moments for transitions to the two diabatic states are equal in magnitude by symmetry. Their orientation depends on the geometry of the molecule. The projection of the transition dipole moments in the *xz* plane for an M−B−M-type molecule is shown in Figure 3.

The relative orientation between the dipoles is defined by the angle β. When β equals 180°, the dipoles are oriented in opposite directions along the *x* axis and thus are opposite in sign. This orientation applies, for example, if the transition to the bridging group occurs from symmetry-equivalent groups linearly oriented on opposite sides of the bridge. In this case, the transitions are described as *antiparallel*. If β equals 0°, the dipoles are oriented in the same direction along the *z* axis and therefore have the same sign. These *parallel* transition dipole moments could result in a nonlinear molecule if the donating groups are on the same side of the bridge. In general, the dipole moments will form an angle between 180° (antiparallel) and 0° (parallel), and the vector components need to be determined. All of these factors determine the selection rules and the relative intensities of the bands as derived below.

The transition dipole moment matrix in the diabatic basis that represents the transition from the ground state to the two diabatic states is

$$\mu = \begin{pmatrix} 0 & \pm\mu_1 & \mu_2 \\ \pm\mu_1 & 0 & 0 \\ \mu_2 & 0 & 0 \end{pmatrix} \qquad (11)$$

The positive signs apply for parallel transitions, and the negative signs apply for antiparallel transitions. The transformation to the adiabatic basis gives

$$\mu = \begin{pmatrix} 0 & \pm\mu_1 \cos\theta + \mu_2 \sin\theta & \mp\mu_1 \sin\theta + \mu_2 \cos\theta \\ \pm\mu_1 \cos\theta + \mu_2 \sin\theta & 0 & 0 \\ \mp\mu_1 \sin\theta + \mu_2 \cos\theta & 0 & 0 \end{pmatrix} \tag{12}$$

where

$$\tan 2\theta = \frac{2H_{ab}^{\text{ex}}}{V_1(Q) - V_2(Q)} \tag{13}$$

The adiabatic state represented by the wave function, $\Psi^+ = \cos\theta\,\Psi_1 + \sin\theta\,\Psi_2$, is the in-phase combination of the diabatic functions. The out-of-phase combination of the diabatic functions is represented in the adiabatic basis by the wave function: $\Psi^- = -\sin\theta\,\Psi_1 + \cos\theta\,\Psi_2$. In the adiabatic basis, the transition dipole to the surface represented by Ψ^+ is $\mp\mu_1 \sin\theta + \mu_2 \cos\theta$. For parallel transition dipole moments, the positive sign applies, and this function is nonzero everywhere along the Q coordinate. The physical meaning is that the transition from the ground state to the adiabatic surface associated with Ψ^+ is electric dipole-allowed (in the adiabatic limit where $H_{ab}^{\text{ex}} \gg V_1(Q) - V_2(Q)$). In contrast, the transition dipole to the state represented by Ψ^- is $\pm\mu_1 \cos\theta + \mu_2 \sin\theta$. The negative sign applies for parallel dipole moments, and this function is zero at $Q = 0$ but is positive when $Q > 0$ and negative when $Q < 0$. The physical meaning is that the transition is electric dipole-forbidden at the internuclear equilibrium geometry but is vibronically allowed. In the case of antiparallel transition dipole moments, the signs are reversed; the transition to the surface represented by Ψ^+ is dipole-forbidden and that to the surface represented by Ψ^- is dipole-allowed. The relative energies of these two states are determined by the sign of H_{ab}^{ex}, which will be discussed in detail in the next section.

In general, transition dipole moments will be neither completely parallel nor completely antiparallel but instead will have vector components in both directions. A sketch of dipole moments relevant to $\mathbf{1}^+$ is shown in Figure 3**.** The transition dipole moment vectors have an angle β between them where $0° \le \beta \le 180°$. For randomly oriented molecules and unpolarized light, the relative intensities of the low- and high-energy transitions will be determined by the vector projections of dipoles on the parallel and antiparallel directions as shown in Figure 3. In this figure, the direction of the parallel dipoles is defined as the $+z$ axis and that for the antiparallel dipoles as the $\pm x$ axis. The ratio of the parallel to antiparallel transition dipole components μ_p and μ_a (i.e., the ratio of the projections on the z and x axes, respectively) is

$$\frac{\mu_a}{\mu_p} = \frac{\mu \sin\dfrac{\beta}{2}}{\mu \cos\dfrac{\beta}{2}} = \tan\frac{\beta}{2} \tag{14}$$

Thus, the ratio of the oscillator strengths of the parallel and antiparallel components, f_p and f_a, is given by

$$\frac{f_a}{f_p} = \frac{\mu_a^2}{\mu_p^2} = \left(\tan\frac{\beta}{2}\right)^2 \tag{15}$$

where

$$f = C\int \frac{\epsilon(\omega)}{\omega}\,\mathrm{d}\omega \tag{16}$$

The spectrum of randomly oriented molecules will be a superposition of the parallel and antiparallel spectra, and the ratio of the absorptivities of the two bands will be given by eq 15.

4. Sign of the Coupling, H_{ab}^{ex}. The coupling between the two diabatic states can be either positive or negative. The sign of the coupling is rarely considered in electron-transfer spectroscopy because it does not affect ground-state intervalence spectra or electron transfer rates. However, the sign has a profound influence on excited-state mixed-valence spectroscopy because it determines the identities of the lowest- and highest-energy adiabatic states. The interactions of pairs of orbitals through bonds have been the subject of theoretical and experimental investigation[37−50] following the pioneering work of Hoffmann et al.[37] Theoretical investigations include relative signs of through-bond and through-space interactions,[37−39] counterintuitive orbital mixing,[40] and quantitative aspects calculated using MO methods.[37,40−42] Experimental applications include splittings measured by photoelectron spectroscopy[37,41,43,44] and electron or hole transport.[39,45] In this section, a simple method for calculating the sign of the coupling inspired by Hoffmann's analyses is presented. This method, named the neighboring orbital model, is used to derive the effect of the sign on the transition oscillator strengths. Relationships to group theoretically derived selection rules are also presented in this section.

The sign of the coupling determines which adiabatic state is lowest and which is highest in energy. The energy of the adiabatic state represented by the wave function Ψ^+ is $E^+ = (V_1 + V_2)/2 + H_{ab}^{\text{ex}}$. If the coupling, H_{ab}^{ex}, is negative, then this adiabatic state is lower in energy than that represented by Ψ^- with energy $E^- = (V_1 + V_2)/2 - H_{ab}^{\text{ex}}$. Given the selection rules derived in the previous section, the absorption spectrum of a molecule with parallel transition dipole moments ($\beta = 0°$) and negative coupling will consist of a strong low-energy band and a weak high-energy band separated by twice the coupling. A molecule with antiparallel transition dipole moments ($\beta = 180°$) and negative coupling will have an absorption spectrum consisting of a weak low-energy band and a strong high-energy band separated by twice the coupling. If the sign of the coupling is positive, the relative energies of the adiabatic states are reversed. In other words, the adiabatic state represented by the wave function Ψ^- is lower in energy than that represented by Ψ^+. With positive coupling, a molecule with parallel transition dipole moments will have an absorption spectrum consisting of a weak low-energy band and a strong high-energy band, and a molecule with antiparallel transition dipole moments will have an absorption spectrum consisting of a strong low-energy band and a weak high-energy band.

What determines the sign of the coupling? For through-space coupling, the sign is intrinsically negative. The reason is reminiscent of simple MO theory where the in-phase overlap between two orbitals produces a bonding molecular orbital (no nodes), and the exchange integral β is thus defined as negative. However, when the coupling is mediated by other orbitals in a molecule, the sign can be positive. A simple physical representation that is relevant to $\mathbf{1}^+$ is shown in Figure 4.

In this molecule, the coupling between the phenyl groups is mediated by neighboring orbitals from the intervening hydrazine bridge, because the phenyl groups are too far apart to have significant through-space coupling. The most important of those orbitals are those closest in energy to the phenyl orbitals, because mixing will be greatest. The appropriate phenyl π orbitals contain one node, as shown in the figure. These two orbitals

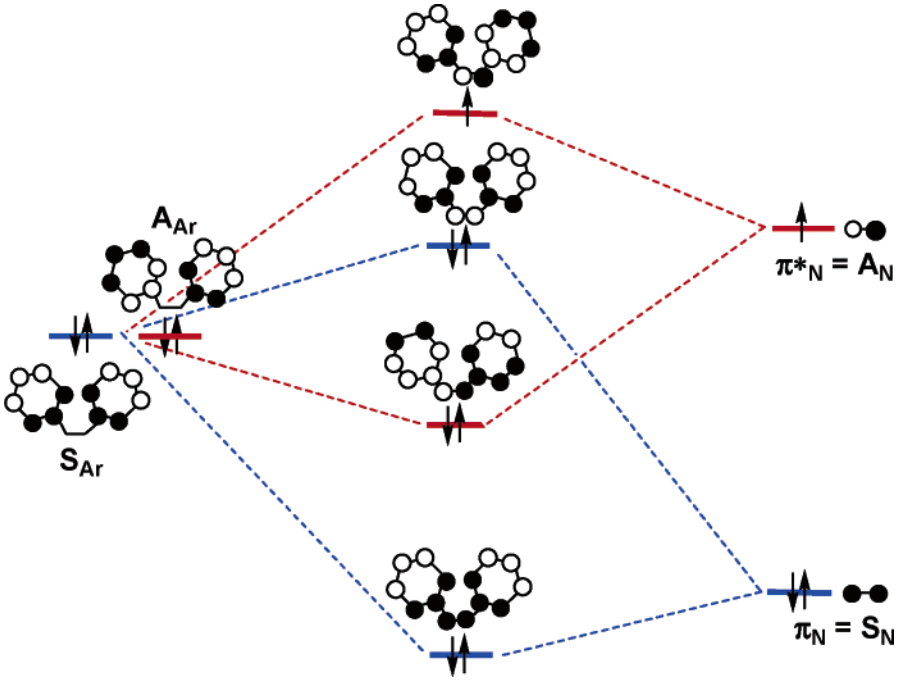

Figure 4. Neighboring orbital model for $\mathbf{1}^+$. The NN π and π^* bridging orbitals appear on the right and the in- and out-of-phase linear combination of phenyl π orbitals appear with equal energies on the left. The molecular orbitals after mixing appear in the center. The phenyl rings are illustrated in the same plane to most clearly indicate the nodal planes in the molecular orbitals.

are degenerate and, in the absence of coupling, can be represented either by the π system of the phenyl on the left and that of the phenyl on the right or by linear combinations of the left and right π systems. The linear combinations are in-phase $\pi_{Ph} + \pi_{Ph}$ (labeled as S_{Ar}) or out-of-phase $\pi_{Ph} - \pi_{Ph}$, A_{Ar}. The bridge orbitals of interest are the NN π bonding and the NN π antibonding orbitals. The NN π bonding orbital has the appropriate symmetry to mix with the in-phase combination, $\pi_{Ph} + \pi_{Ph}$, and the NN π antibonding orbital has the appropriate symmetry to mix with the out-of-phase combination, $\pi_{Ph} - \pi_{Ph}$. When the orbitals of the same symmetry mix, the degeneracy of the linear combinations, $\pi_{Ph} + \pi_{Ph}$ and $\pi_{Ph} - \pi_{Ph}$, is removed. As illustrated by the molecular orbitals at the center of Figure 4, the energy of the molecular orbital containing the $\pi_{Ph} + \pi_{Ph}$ combination is higher than that containing the $\pi_{Ph} - \pi_{Ph}$ combination. This is the opposite order from that expected if the usual through-space coupling was operative. Therefore, the coupling is positive. The energy ordering of the molecular orbitals obtained using this simple analysis is verified by DFT MO calculations.

The above analysis provides a simple physical picture of the origin of the sign of the coupling. When two diabatic states are coupled and the coupling is mediated by intervening orbitals from a bridging group, the sign of the coupling can be either positive or negative.

Group Theory and Physical Picture. The selection rules for the different polarization directions can be explained independently using group theory. The point group of the molecule is C_2. The "in-phase" linear combination of the phenyl π orbitals has *b* symmetry in this point group and the "out-of-phase" linear combination has *a* symmetry. As previously discussed, each linear combination mixes with the NN π orbital of the same symmetry, as shown in Figure 4. If this set of molecular orbitals for $\mathbf{1}^+$ is used, the ground-state electron configuration is $(b)^2(a)^2(b)^2(a)^1$. The irreducible representation of the ground state is ^{2}A. The transition from the ground state to the first excited state (^{2}B symmetry) is allowed in *x* polarization. This direction corresponds to antiparallel transition dipoles (i.e., the component of the transition dipole along the *x* direction). The transition from the ground state to the second excited state (^{2}A symmetry) is allowed in *z* polarization. These selection rules for the different polarization directions are illustrated schematically by the probability contour diagrams in Figure 5.

The transition dipole moment is given by $\hat{\mu}_{eg} = \int \Psi_e e r^{\varpi} \Psi_g \, d\mathbf{r}$ where the electric dipole moment operator, er^{ϖ}, is represented in Figure 5 by a function that changes sign at the origin along the *z* or *x* axis. The ground state is represented by a hole in the highest-energy molecular orbital of Figure 4. For the *x* component of the electric dipole operator, $er^{\varpi}\Psi_g$ is represented by the ground-state wave function with a change of phase at the origin along the *x* axis where the negative sign is to the left of the *yz* plane. The third row of Figure 5 shows the excited-state wave function, which is represented by the hole in the higher-energy molecular orbital with the in-phase phenyl π system. The pictorial representation of the transition dipole moment, $\int \Psi_e e r^{\varpi} \Psi_g \, d\mathbf{r}$, is illustrated in the bottom row as the overlap of $er^{\varpi}\Psi_g$ with Ψ_e. The overlap is nonzero, representing an allowed transition. Similar pictures are used for *z* polarization in the bottom panel of Figure 5. The physical meaning derived from these overlap functions is the selection rules for the two excited-state mixed-valence transitions in the two polarization directions. The lower-energy transition from the ground state to the excited state represented by the molecular orbital with the in-phase phenyl π system is allowed in the *x* polarized direction, where the *x* direction corresponds to the antiparallel component of the transition dipole moment. Similarly, the higher-energy transition from the ground state to the excited state represented by the molecular orbital with the out-of-phase phenyl π system is allowed in the *z* polarized direction, where the *z* direction corresponds to the parallel component of the transition dipole moment. It is important to note that the difference in energy between the ^{2}A and ^{2}B excited states is the same as the energy difference produced by the H_{ab}^{ex} coupling term. This correlation between the mixing of neighboring orbitals and the effective coupling it produces will be further addressed in future publications.

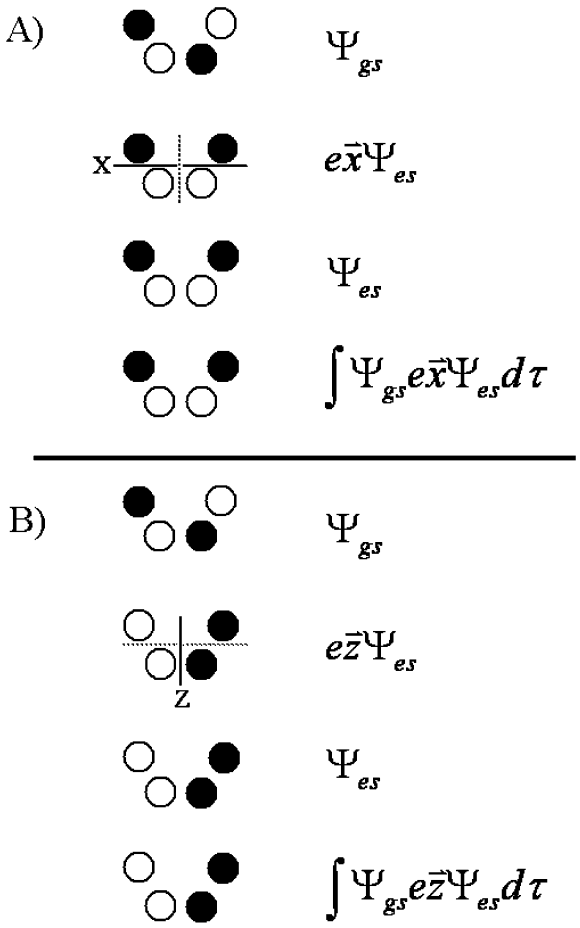

Figure 5. Top line: Ground-state wave function (hole formalism). Second line: Interaction of ground-state wave function with the vector potential of light (*x*-polarized in the top panel and *z*-polarized in the bottom panel) which places a node in the wave function. Third line: Excited-state wave functions (*b* symmetry in the top panel and *a* symmetry in the bottom panel). Fourth line: Nonzero overlap between lines 2 and 3 illustrating the nonzero transition dipole moment.

5. Important Symmetric Modes from Resonance Raman Spectra. The symmetric modes provide the majority of the bandwidths of the absorption and emission spectra. The key factor in absorption bandwidth is the slope of each excited-state surface in the Franck−Condon region. The slope is determined by both the frequency and displacement of the potential surface along its normal coordinate. The frequencies of the excited-state surfaces along the symmetric coordinates are determined from the resonance Raman spectrum. The displacements are determined by the intensities. Raman spectra of $\mathbf{1}^+$ were obtained in resonance with both the high- and low-energy components of the absorption band. The vibrational frequencies are the same, but the intensity ratios and therefore the displacements along the symmetric coordinates are slightly different. If the system is treated in the adiabatic limit, the interpretation of the different intensity ratios leads to two different sets of displacements along the symmetric coordinates, one associated with the upper adiabatic excited state and the other associated with the lower adiabatic excited state. However, the overlap of the higher-energy component (i.e., the transition to the upper adiabatic) with next higher-energy absorption band attributed to the bridge-centered π-to-π^* transition cannot be ignored. The resonance Raman intensities that occur when in resonance with the higher-energy component are influenced by the interference with this higher-energy band.[51] Consequently, the displacements of the symmetric modes used in the absorption and emission calculations were carried out using the intensity ratios of the Raman spectrum in resonance with the lower-energy component. This band is low enough in energy so that overlap with the $\pi-\pi^*$ band is negligible. Although it is possible that the displacements along the symmetric coordinates do vary with respect to the upper and lower adiabatic surfaces, using one set of symmetric mode displacements is a good approximation for fitting the unstructured components of the absorption band.

Vibrational assignments are made by comparing the calculated vibrational modes with the observed resonance Raman frequencies as presented in Table 1. The symmetric modes below 600 cm^{-1} involve significant C−N−N−C twist-angle change, and those between 619 and 1000 cm^{-1} involve phenyl ring deformation and rocking. The modes at 1188 and 1205 cm^{-1} are assigned to symmetric C−N stretching modes, and the mode at 1413 cm^{-1} is assigned to a symmetric mode with significant N−N stretching character. The highest-energy modes at 1489 and 1586 cm^{-1} involve phenyl ring CC stretching.

The structural changes that $\mathbf{1}^+$ experiences in the mixed-valence excited state are explained by the resonance Raman data and vibrational assignments outlined in Table 1. Resonance Raman spectroscopy shows enhancement of many low-frequency modes assigned as C−N−N−C twisting modes. Higher-frequency modes involving either C−N or N−N stretches or both also show significant displacement. These structural changes are consistent with those expected for this type of electronic transition. On the basis of the MO calculations for $\mathbf{1}^+$, the higher-energy electronic transition occurs from a molecular orbital that is bonding across the two C−N bonds to an orbital that is antibonding across C−N. Consequently, significant C−N bond length changes are expected to occur upon excitation. Similarly, the lower-energy electronic transition occurs from a molecular orbital that is bonding across the bridge to an orbital that is antibonding across the bridge. Therefore, a change in the N−N bond length is expected in the excited state. Because this electronic transition also promotes a change in nitrogen hybridization from sp^2 to sp^3, modes involving the C−N−N−C twist angle change are expected to be important.

6. Calculated Fit of Absorption, Emission, and Resonance Raman Spectra. After a brief explanation of the steps involved in the calculations, the parameters chosen to define the ground- and excited-state surfaces and the calculated fits to the electronic spectra are discussed. The experimental emission of $\mathbf{1}^+$ is compared to that of the monophenyl species.

As previously discussed, the absorption spectrum of $\mathbf{1}^+$ is a superposition of parallel and antiparallel spectra. Consequently, the calculated fit involves the sum of two spectra, one calculated using parallel transition dipole moments and the other using antiparallel transition dipole moments. The parameters that describe the ground- and excited-state surfaces (diabatic frequency, displacement, and coupling) along the asymmetric and symmetric coordinates are identical for the two calculations. The sum is weighted by the vector projections of the dipoles in the parallel and antiparallel directions to obtain the appropriate intensity ratio of the two components of the absorption band. The weighted sum involves a scaling factor which equals $\tan^2(\beta/2)$ according to eq 15.

To calculate the spectra, appropriate parameters must be chosen to define the ground- and excited-state surfaces. First, the frequency must be chosen for the asymmetric mode of the excited-state mixed-valence surfaces. The asymmetric modes of $\mathbf{1}^+$ are not expected to undergo significant enhancement in the resonance Raman spectrum. Therefore, only frequencies of modes that are exclusively IR-active were considered in defining

the ground- and excited-state surfaces along the asymmetric coordinate. The phenyl-to-hydrazine transition is expected to involve (phenyl)C−N stretching modes as well as CNNC twist modes. The resonance Raman data in Table 1 show that the symmetric modes that undergo the biggest distortions are the low-frequency CNNC twist modes. The asymmetric CNNC twist modes are expected to have similar distortions and occur in the same frequency region as their symmetric-mode counterparts, which occur around 500 cm^{-1}. Therefore, from the experimental IR data, we chose the 542 cm^{-1} frequency to define the ground-state harmonic potential surface along the asymmetric coordinate. This choice is further supported by the MO calculation for this molecule, which yields an asymmetric normal mode at 487 cm^{-1} involving significant change in the CNNC twist angle. The coupling is defined by the peak separation in the experimental absorption spectrum. The optimal H_{ab}^{ex} for the diabatic surfaces along the asymmetric coordinate is 3750 cm^{-1}. Changing this value by more than ±100 cm^{-1} results in significantly poorer calculated spectra.

The value of H_{ab}^{ex} is determined from experiment (i.e., from the splitting in the absorption spectrum), whereas Δ is not. Because resonance enhancement of the asymmetric modes in this molecule is extremely small, we cannot use resonance Raman intensity to obtaining a value for the displacement. The value of Δ, however, must be large enough so that the resulting structural changes for the vibrational mode are comparable to those associated with the symmetric modes for the same transition, yet small enough so that, with the experimentally determined coupling, the lower adiabatic surface possesses a single minimum, thus preserving the delocalization of the charge in the excited state. Because the asymmetric Δ value is not defined experimentally, we chose a value of 0.8, which is comparable to the Δ values of similar symmetric modes.

The absorption spectrum calculation includes both the asymmetric and symmetric coordinates. The frequencies and displacements of the symmetric modes are presented Table 1 and were discussed in section 5. The vibrational reorganization energy, λ_V^{ex} is 1586 cm^{-1} (the sum of the symmetric values from the resonance Raman experiment and the asymmetric value). Even after including the solvent component of the total reorganization energy, $\lambda^{ex}/2$ is substantially smaller than H_{ab}^{ex} (3750 cm^{-1}) and consistent with the charge remaining delocalized in the excited state.

With these parameters defining the ground- and excited-state surfaces along the symmetric and asymmetric coordinates, the parallel and antiparallel spectra are calculated separately. After the antiparallel spectrum is scaled by a factor of 2.85, the two spectra are added, rendering the total spectrum. For the calculated fit of the room-temperature absorption spectrum, $\Gamma = 1500$ cm^{-1}. The scaled parallel and antiparallel calculated absorption spectra along with the total spectrum are presented in Figure 6 (top). As the figure reveals, the two components of the total calculated absorption spectrum occur at the appropriate energies and have the necessary intensity ratio and bandwidths to fit the experimental spectrum. The combination of the symmetric and asymmetric modes is required to produce the overall bandwidth and band shape. On the basis of the ground-state geometry, where the nitrogens have approximately sp^2 hybridization, the angle between the two transition dipole moments, β, was expected to be about 120°. If eq 15 is used with the absorptivity ratio from the calculated spectra, β is calculated to be 119°.

Emission Spectra. Using the same parameters that define the ground- and excited-state surfaces for the calculation of the absorption spectrum, one can obtain the lowest-energy eigenfunction of the excited-state surface . After multiplying this eigenfunction by the appropriate transition dipole moment, the resulting initial wave packet, ϕ_i, is then propagated on the ground-state potential surface. The time-dependent overlap, $\langle\phi_i|\phi(t)\rangle$, is calculated and used to generate the emission spectrum, shown in Figure 6 (bottom panel). The fit of the 15 K emission spectrum includes a damping factor, Γ, of 400 cm^{-1}.

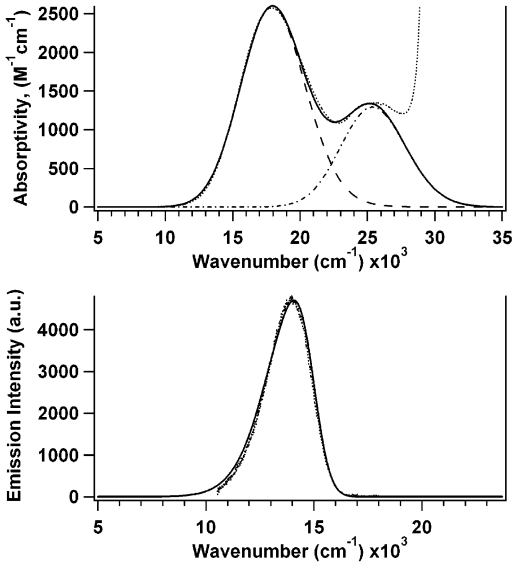

Figure 6. Top panel: Calculated fit (solid line) of the experimental absorption spectrum (dotted line), which is the superposition of spectra calculated with parallel (dot−dashed line) and antiparallel (dashed line) transition dipole moments. Bottom panel: Calculated fit (solid line) of experimental emission spectrum (dotted line).

It is of interest to compare the diphenyl cation experimental emission spectrum with that of the monophenyl species. Figure 1 illustrates that the emission spectrum of $\mathbf{1}^+$ is red-shifted compared to that of $\mathbf{2}^+$, consistent with the trend of the absorption spectra of the two compounds. The emission bandwidth of $\mathbf{1}^+$ is nearly one-half that of $\mathbf{2}^+$. This is explained by the difference in the excited-state surfaces of the two species. The strong coupling of $\mathbf{1}^+$ yields a single minimum in the excited-state lower adiabatic surface, which is positioned at $Q = 0$ along the asymmetric normal coordinate. Consequently, when the excited-state wave packet undergoes a vertical transition to the ground state, it experiences essentially zero slope and a narrow emission spectrum results. The emission spectrum of the monophenyl species has a wider bandwidth, because the uncoupled excited-state surface is displaced relative to the ground-state surface, and the excited-state wave packet in this case experiences a nonzero slope upon vertical transition to the ground state. The symmetric modes, which were discussed in the previous section, also contribute to the width of the emission spectra of both species.

7. Summary

An excited-state mixed-valence model is used to explain the electronic transition of the diphenyl cation, $\mathbf{1}^+$, a phenyl-to-hydrazine charge transfer. The absorption band consists of 2 components resulting from the transition to the coupled excited state. Emission from the lowest-energy vibronic level of the coupled excited state to the ground state is observed at low temperature. Band intensities in the resonance Raman spectra are used to determine the displacements of the totally symmetric normal modes. The absorption, emission, and resonance Raman

spectra are fit simultaneously by using the 18 dimensional potential energy surfaces (17 symmetric coordinates, 1 asymmetric coordinate). The time-dependent theory of spectroscopy and methodology are designed to calculate spectra involving coupled surfaces and are exact quantum calculations using the model Hamiltonian.

The energy separation between the two components of the absorption spectrum is a consequence of the magnitude of the excited-state coupling. When coupling is mediated by intervening orbitals from a bridging group, the sign of the coupling can be either positive or negative. The sign of the excited-state coupling is explained using a neighboring orbital model, which focuses on the molecular orbitals on the bridge that mix with the orbitals on the phenyl groups. The coupling in $\mathbf{1}^+$ is positive, because after the phenyl and bridging orbitals of appropriate symmetry mix, the resulting MO with the out-of-phase combination of the phenyl π systems is lower in energy than the in-phase combination.

The intensity ratio of the two components of the absorption spectrum is also related to the orientation of the transition dipole moments. The transition dipole moments associated with the phenyl-to-hydrazine electron transfer of $\mathbf{1}^+$ consist of parallel and antiparallel vector components. In the diabatic basis, the transition dipoles in the antiparallel direction have opposite signs, whereas the dipoles in the parallel direction have the same signs. Upon transformation to the adiabatic basis with positive coupling, the dipole moment at the ground-state internuclear separation for the transition to the higher-energy adiabatic surface is nonzero for the parallel component and zero for the antiparallel component. Conversely, the dipole moment for the transition to the lower-energy adiabatic surface is zero for the parallel component and nonzero for the antiparallel component. The absorption spectrum is the sum of the spectra calculated using parallel and antiparallel transition dipole moments weighted by the vector projections of the dipoles in the parallel and antiparallel directions.

The structural changes that the diphenyl cation experiences upon excitation are calculated from the resonance Raman intensities. The most highly distorted symmetric modes involve CNNC twisting motion in the low-frequency region and C−N and N−N distortions in the higher-frequency region. These changes are consistent with the phenyl-to-hydrazine charge transfer assignment, because the transition involves molecular orbitals that change bonding character across the C−N and N−N bonds. In addition, the electronic transition involves a change in nitrogen hybridization from approximately sp^2 to sp^3. The largest structural change that the diphenyl cation experiences is in fact a CNNC twist.

Excited-state mixed valence, although not investigated in detail until now, is expected to be an important contributor to the electronic spectra of many organic and inorganic compounds. The spectra will provide new information for understanding coupling in mixed-valence systems. The signature of a mixed-valence excited state is an absorption band consisting of two components. The energy separation between these two components is a direct measure of the magnitude of coupling, and the relative intensities of the two bands are governed by the details of the transition dipole moments.

Acknowledgment. This work was made possible by grants from the National Science Foundation (CHE0206857 to J.I.Z. and CHE0240197 to S.F.N.).

Supporting Information Available: X-ray structures of **1** (**22/Ph2**) and $\mathbf{1}^+$ ($\mathbf{SbF_6}^-$). This material is available free of charge via the Internet at http://pubs.acs.org.

References and Notes

(1) Lockard, J. V.; Zink, J. I.; Konradsson, A. E.; Weaver, M. N.; Nelsen, S. F. *J. Am. Chem. Soc.* **2003**, *125*, 1347.
(2) (a) Hush, N. S. *Prog. Inorg. Chem.* **1967**, *8*, 391. (b) Hush, N. S. *Coord. Chem. Rev.* **1985**, *64*, 135.
(3) (a) Sutin, N. *Prog. Inorg. Chem.* **1983**, *30*, 441. (b) Marcus, R. A.; Sutin, N. *Biochim. Biophys. Acta* **1985**, *811*, 265.
(4) Lee, S.-Y.; Heller, E. J. *J. Chem. Phys.* **1979**, *71*, 4777.
(5) Heller, E. J. *Acc. Chem. Res.* **1981**, *14*, 368.
(6) Heller, E. J.; Sundberg, R. L.; Tannor, D. *J. Phys. Chem.* **1982**, *86*, 1822.
(7) Myers, A. B. In *Laser Techniques in Chemistry*; Wiley: New York, 1995; Vol. 23, p 325.
(8) Zink, J. I.; Shin, K.-S. K. In *Advances in Photochemistry*; Wiley: New York, 1991; Vol. 16, p 119.
(9) Reber, C.; Zink, J. I. *Comments Inorg. Chem.* **1992**, *13*, 177.
(10) Wexler, D.; Zink, J. I.; Reber, C. In *Electronic and Vibronic Spectra of Transition Metal Complexes I*; Yersin, H., Ed.; Springer-Verlag: Berlin, 1994; p 174.
(11) Pelletier, Y.; Reber, C. *Inorg. Chem.* **1997**, *36*, 721.
(12) Bussière, G.; Reber, C. *J. Am. Chem. Soc.* **1998**, *120*, 6306.
(13) Bussière, G.; Beaulac, R.; Cardinal-David, B.; Reber, C. *Coord. Chem. Rev.* **2001**, *219*−*221*, 509.
(14) Reber, C.; Zink, J. I. *J. Chem. Phys.* **1992**, *96*, 2681.
(15) Neuhauser, D.; Park, T. J.; Zink, J. I. *Phys. Rev. Lett.* **2000**, *85*, 5304.
(16) Landry-Hum, J.; Tessier, V.; Ernzerhof, M.; Reber, C. *Coord. Chem. Rev.* **2002**, *233*−*234*, 65.
(17) Schenker, R.; Triest, M.; Reber, C.; Güdel, H. U. *Inorg. Chem.* **2001**, *40*, 5787.
(18) Bussière, G.; Reber, C.; Neuhauser, D.; Walter, D. A.; Zink, J. I. *J. Phys. Chem. A* **2003**, *107*, 1258.
(19) Reber, C.; Zink, J. I. *J. Phys. Chem.* **1992**, *96*, 571.
(20) Simoni, E.; Reber, C.; Talaga, D.; Zink, J. I. *J. Phys. Chem.* **1993**, *97*, 12678.
(21) Talaga, D. S.; Zink, J. I. *J. Phys. Chem.* **1996**, *100*, 8712.
(22) Talaga D. S.; Zink, J. I. *J. Phys Chem. A* **2001**, *105*, 10511.
(23) Nelsen, S. F.; Ismagilov, R. F.; Powell, D. R. *J. Am. Chem. Soc.* **1996**, *118*, 6313.
(24) Nelsen, S. F.; Chen, L. J.; Petillo, P. A.; Evans, D. H.; Neugebauer, F. A. *J. Am. Chem. Soc.* **1993**, *115*, 10611.
(25) Neugebauer, F. A.; Wegner, H. *Chem. Ber.* **1979**, *112*, 1076.
(26) Frisch, M. J.; Trucks, G. W.; Schlegel, H. B.; Scuseria, G. E.; Robb, M. A.; Cheeseman, J. R.; Zakrzewski, V. G.; Montgomery, J. A., Jr.; Stratmann, R. E.; Burant, J. C.; Dapprich, S.; Millam, J. M.; Daniels, A. D.; Kudin, K. N.; Strain, M. C.; Farkas, O.; Tomasi, J.; Barone, V.; Cossi, M.; Cammi, R.; Mennucci, B.; Pomelli, C.; Adamo, C.; Clifford, S.; Ochterski, J.; Petersson, G. A.; Ayala, P. Y.; Cui, Q.; Morokuma, K.; Malick, D. K.; Rabuck, A. D.; Raghavachari, K.; Foresman, J. B.; Cioslowski, J.; Ortiz, J. V.; Stefanov, B. B.; Liu, G.; Liashenko, A.; Piskorz, P.; Komaromi, I.; Gomperts, R.; Martin, R. L.; Fox, D. J.; Keith, T.; Al-Laham, M. A.; Peng, C. Y.; Nanayakkara, A.; Gonzalez, C.; Challacombe, M.; Gill, P. M. W.; Johnson, B. G.; Chen, W.; Wong, M. W.; Andres, J. L.; Head-Gordon, M.; Replogle, E. S.; Pople, J. A. *Gaussian 98*; Gaussian, Inc.: Pittsburgh, PA, 1998.
(27) (a) Becke, A. D. *J. Chem. Phys.* **1993**, *98*, 5648. (b) Becke, A. D. *Phys. Rev. A* **1988**, *38*, 3098. (c) Lee, C.; Yang, W.; Parr, R. G. *Phys. Rev. B* **1988**, *37*, 785. (d) Vosko, S. H.; Wilk, S. H.; Nusair, M. *Can. J. Phys.* **1980**, *58*, 1200.
(28) *Jaguar*, Version 4.1; Schrodinger, Inc.: Portland, OR, 2000.
(29) *Spartan '02*; Wavefunction, Inc.: Irvine, CA, 2002.
(30) Schaftenaar, G.; Noordik, J. H. Molden: a pre- and post-processing program for molecular and electronic structures. *J. Comput.-Aided Mol. Design* **2000**, *14*, 123−134.
(31) Zhang, J. Z.; Heller, E. J.; Huber, D.; Imre, D. G. *J. Phys. Chem.* **1991**, *95*, 6129.
(32) Alvarellos, J.; Metiu, H. *J. Phys. Chem.* **1988**, *88*, 4957.
(33) Jiang, X. P.; Heather, R.; Metiu, H. *J. Chem. Phys.* **1989**, *90*, 6903.
(34) Heather, R.; Metiu, H. *J. Chem. Phys.* **1992**, *96*, 2681.
(35) Nelsen, S. F.; Ismagilov, R. F.; Powell, D. R. *J. Am. Chem. Soc.* **1997**, *119*, 10213.
(36) Nelsen, S. F.; Tran, H. Q.; Ismagilov, R. F.; Ramm, M. T.; Chen, L.-J.; Powell, D. R. *J. Org. Chem.* **1998**, *63*, 2536.
(37) Hoffman, R. *Acc. Chem. Res.* **1971**, *4*, 1.
(38) Verhoeven, J. W.; Pasman, P. *Tetrahedron* **1981**, *37*, 943.
(39) Paddon-Row, M. N.; Shephard, M. J. *J. Am. Chem. Soc.* **1997**, *119*, 5355.
(40) Whangbo, M. H.; Hoffman, R. *J. Chem. Phys.* **1978**, *68*, 5498.

(41) Marsman, A. W.; Havenith, R. W. A.; Bethke, S.; Jenneskens, L. W.; Gleiter, R.; van Lenthe, J. H. *Eur. J. Org. Chem.* **2000**, *14*, 2629.
(42) Heilbronner, E.; Schmelzer, A. *Helv. Chim. Acta* **1975**, *58*, 936.
(43) Dougherty, D.; Brint, P.; McGlynn, S. P. *J. Am. Chem. Soc.* **1978**, *100*, 5597.
(44) Gleiter, R.; Lange, H.; Borzyk, O. *J. Am. Chem. Soc.* **1996**, *118*, 4889.
(45) Newton, M. D. *Chem. Rev.* **1991**, *91*, 767.
(46) Paddon-Row, M. N. *Acc. Chem. Res.* **1982**, *15*, 245.
(47) Gleiter, R.; Schaifer, W. *Acc. Chem. Res.* **1990**, *23*, 369.
(48) De Ridder, D.; Goubitz, K.; Shenk, H.; Krijnen, B.; Verhoeven, J. W. *Helv. Chim. Acta* **2003**, *86*, 799.
(49) Sarneel, R.; Worrell, C. W.; Pasman, P.; Verhoeven, J. W.; Mes, G. F. *Tetrahedron* **1980**, *36*, 3241.
(50) Imamura, A.; Ohsaku, M. *Tetrahedron* **1981**, *37*, 2191.
(51) Reber, C.; Zink, J. I. *J. Phys. Chem.* **1992**, *96*, 571.